

Cracking and bending strength evaluations of steel-concrete double composite girder under negative bending action

Chen Xu¹, Boyu Zhang¹, Siwei Liu² and Qingtian Su^{*1}

¹Department of Bridge Engineering, Tongji University, Shanghai, China

²Shanghai Municipal Engineering Design Institute(Group) Co., Ltd., Shanghai, China

(Received March 25, 2019, Revised January 14, 2020, Accepted April 10, 2020)

Abstract. The steel-concrete double composite girder in the negative flexural region combines an additional concrete slab to the steel bottom flange to prevent the local steel buckling, however, the additional concrete slab may lower down the neutral axis of the composite section, which is a sensitive factor to the tensile stress restraint on the concrete deck. This is actually of great importance to the structural rationality and durability, but has not been investigated in detail yet. In this case, a series of 5.5 m-long composite girder specimens were tested by negative bending, among which the bottom slab configuration and the longitudinal reinforcement ratio in the concrete deck were the parameters. Furthermore, an analytical study concerning about the influence of bottom concrete slab thickness on the cracking and sectional bending-carrying capacity were carried out. The test results showed that the additional concrete at the bottom improved the composite sectional bending stiffness and bending-carrying capacity, whereas its effect on the concrete crack distribution was not obvious. According to the analytical study, the additional concrete slab at the bottom with an equivalent thickness to the concrete deck slab may provide the best contributions to the improvements of crack initiation bending moment and the sectional bending-carrying capacity. This can be applied for the design practice.

Keywords: double composite action; negative flexural region; cracking moment; bending-carrying capacity; structural rationality

1. Introduction

The steel-concrete composite girder consisting of a concrete slab, a steel girder and shear connectors has been usually applied in bridge structures due to the concrete compression and steel tension merits. And there were also research concerns on the additional contribution of the concrete slab to shear resistance in the combined bending and shear actions (Liang *et al.* 2004). On the other hand, the concrete tension and steel compression in the negative flexural region of a continuous composite girder need to be avoided since they may result in the tensile concrete cracks and steel buckling failure.

The pre-stress operation is one of the typical techniques to eliminate the concrete tension in negative region, whereas the induced steel local buckling should be dealt with carefully in the compression zone (Chen *et al.* 2009). It is influenced by the factors such as the pre-stress force, initial geometrical imperfection and so on (Chen and Jia 2010). Lu and Ji (2018) presented an optimization study on the pre-stress operation on the composite girder with corrugated webs for local buckling prevention and global deflection reduction. Moscoso *et al.* (2017) once presented a numerical simulation to analyze the general mechanical performance of pre-stressed steel concrete composite

beams. Besides the pre-stress operation for the concrete tension elimination, constraining the bending induced tensile crack width by increasing the longitudinal reinforcement ratio is another feasible design method in practice. Furthermore, the fiber reinforced concrete with a favorable tensile performance has been concerned to restrain the concrete cracks so far. Lin *et al.* (2014) and Liang *et al.* (2018) showed the favorable effect of steel fiber reinforced concrete (SFRC) on the crack constraint based on the executed negative bending tests on composite girders. Hamoda *et al.* (2017) provided consistent summations by carrying out four composite girder tests. Xu *et al.* (2017) investigated the favorable effect of SFRC on the static and fatigue behavior of stud shear connector. Nowadays, the ultra high performance concrete with excellent mechanical properties and ductility performance has been increasingly concerned for the crack resistance in the negative flexural region (Shao and Deng, 2016), and the connection detail between the steel and UHPC is being investigated in researches (Wang *et al.* 2018, Wang *et al.* 2019).

Concerning the steel buckling prevention in the compression zone of a negative flexural region, casting and combining additional concrete to the steel bottom flange through connectors is an efficient way. It also helps to form a compact double composite section of which the materials' plasticity can be efficiently utilized. Shim *et al.* (2011) proposed a study on the double composite bridge with high strength steel. Since the local buckling is prevented, the steel high strength can be better utilized. Besides, Kim *et al.*

*Corresponding author, Professor
E-mail: sqt@tongji.edu.cn

Table 1 Specimen detail

Specimens	Composite action	reinforcement ratio	girder length(m)	girder height(m)	connector
NSN-1	normal	1.72%	5.5	0.55	studs
NSN-2	normal	0.86%			
NSD-1	double	1.72%			
NSD-2	double	0.86%			

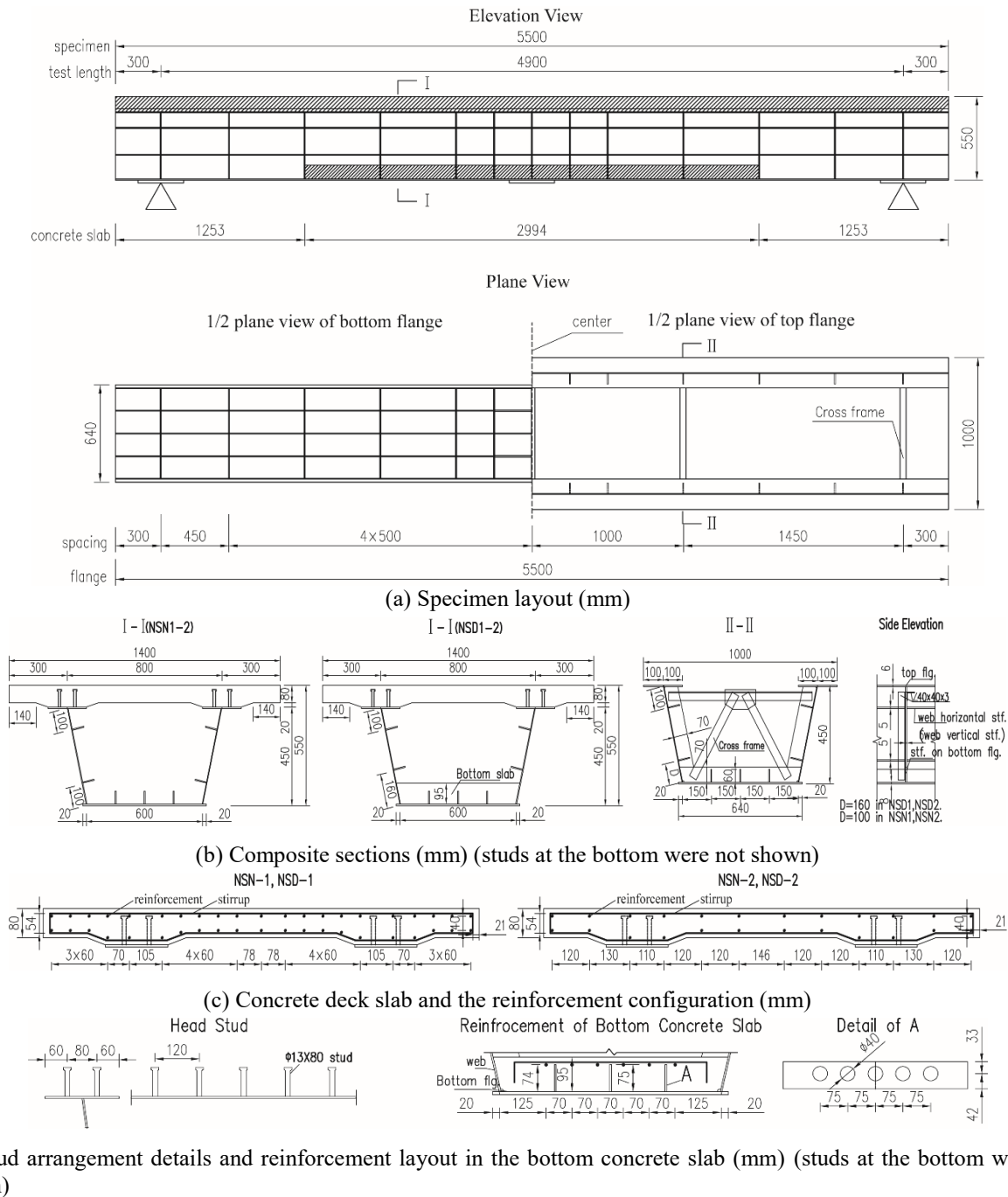


Fig. 1 Specimen layout

(2015) presented a design work of a continuous hybrid girder bridge, including a kind of double composite truss

girder in which the concrete was used in both of the upper and bottom chord. Jiang *et al.* (2016) presented a study on a

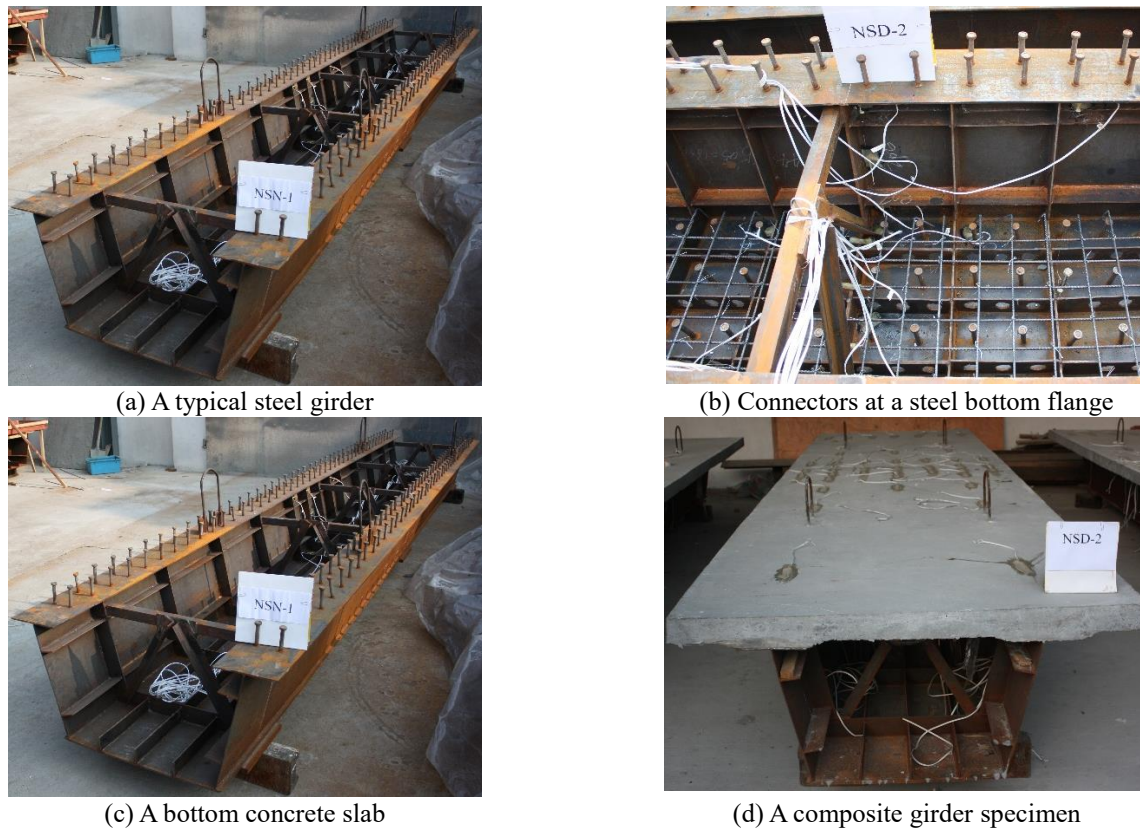


Fig. 2 Specimen photos (By Chen)

continuous composite girder with the web in the negative flexural region encased in the concrete for steel buckling prevention.

Although the double composite action is particularly good to the economical long-span composite bridge design and construction due to its advantage of preventing buckling and increasing the composite sectional bending stiffness (Saul 1996), the additional concrete slab at the bottom can lead to a lower sectional neutral axis height. In other words, the detail effect of double composite action on the tensile cracks of the concrete deck slab remains unclear, and there has been few particular design detail in the codes (AASHTO, 2012; Eurocode 4, 2005; JSCE, 2007; GB50917, 2013) so far. In this case, an experimental study concerning about the effects of double composite action as well as the reinforcement ratio was carried out at first, and then followed by an analytical works on the rational design of additional slab thickness in the double composite section.

2. Experimental setup

2.1 Test specimens

There were four reduced scale steel-concrete composite girder specimens in this study. The specimen design took reference of a 105 m-span continuous composite bridge. As listed in Table 1, the specimens were divided into two groups in terms of the composite section. In addition, the

specimen longitudinal reinforcement ratios were different in each group of specimens.

Fig. 1(a) shows the specimen layout. The full girder length was 5.5 m, including a 0.3 m free extension in each end. As to the specimen with double composite section, a 3.0 m-long extra concrete slab was cast on the steel bottom flange. Its thickness was 95 mm. The braces made of angle bars were installed to resist the specimen lateral deformation.

As shown in Fig. 1(b), the composite girder height was 550 mm, including an 80 mm thick concrete slab with 20 mm thick haunch and a 450 mm high steel tub girder. The thicknesses of the steel top flange, bottom flange and web were 6 mm, 8 mm and 4 mm respectively. The thicknesses of the horizontal and vertical steel stiffeners were 5 mm and 6 mm respectively. And 10 mm thick supporting stiffeners were installed on the steel bottom flange around the loading area.

As shown in Fig. 1(c), the width of concrete deck slab was 1400 mm. There were two layers of longitudinal reinforcements (8 mm in diameter), and the spacing of stirrups (6 mm in diameter) was 80 mm.

Fig. 1(d) shows the shear studs arrangement details. The stud shank diameter and height were 13 mm and 80 mm respectively. The studs were uniformly welded on the steel top flange, the longitudinal and transverse spacing were 120 mm and 80 mm. On the other hand, the studs and perforated ribs were used at the steel bottom flange. The transverse

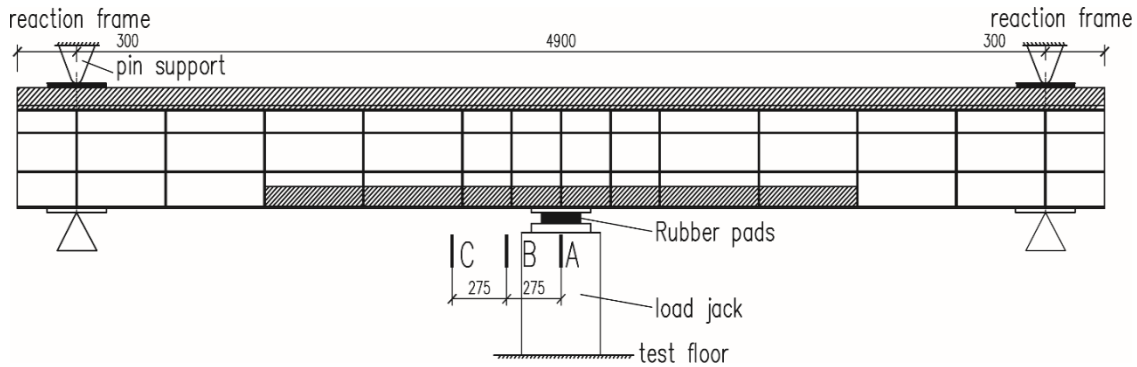
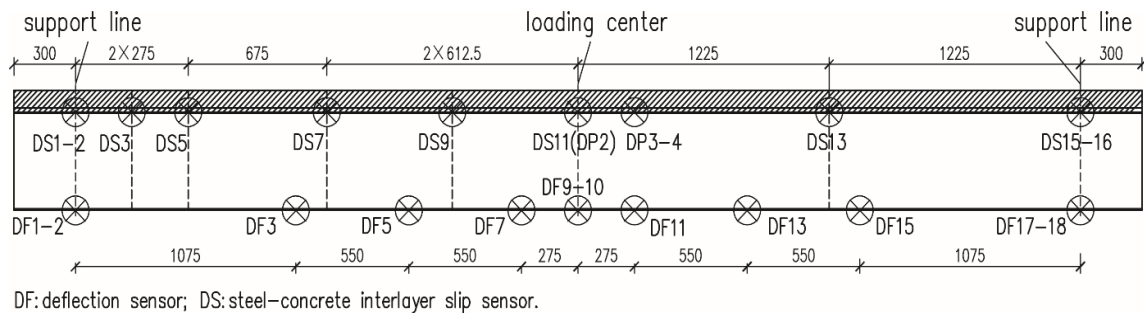


Fig. 3 Load setup and strain investigation positions (mm)



DF: deflection sensor; DS: steel-concrete interlayer slip sensor.

Fig. 4 Sensor positions (mm)

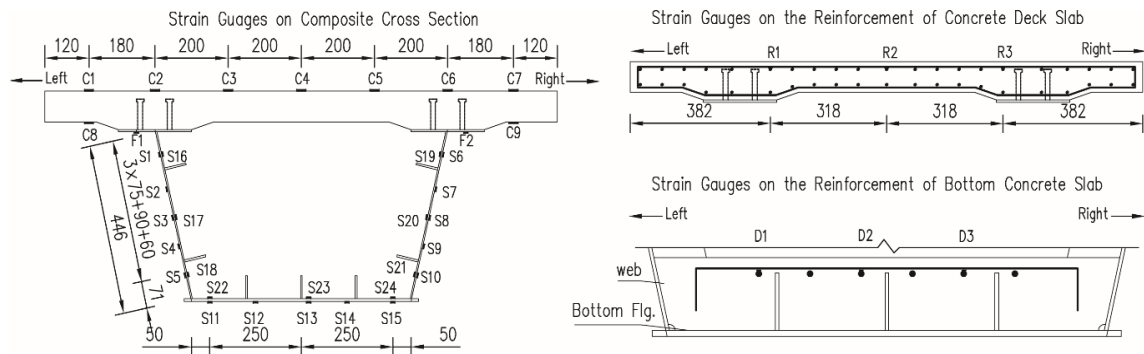


Fig. 5 Strain gauge arrangement in the section at the loading position (Section A-A in Fig.3) (mm)

spacing of the studs on the bottom flange was 150 mm while the longitudinal spacing was 120 mm. In addition, the reinforcement layout in the bottom concrete slab was also depicted in Fig. 1(d).

Fig. 2 presents some specimen photos. Fig. 2(a) shows the steel girder of specimen NSN-1. Fig. 2(b) reflects the connectors of the specimens with double composite sections. Fig. 2(c) shows the bottom concrete slab in the double composite specimen. Fig. 2(d) shows the completed specimen NSD-2.

2.2 Load setup and sensors

Fig. 3 shows the negative bending test setup. A hydraulic jack that placed underneath the girder at the

middle position drove load from the bottom, and there was a 20 mm thick gusset plate placed between the loading jack and the steel bottom flange for the uniform load application on the section. Meanwhile, two pin instruments restrained the specimen ends from the above. The loading procedure included a 60 kN preload process for the test setup confirmation at first and then a monolithic load program to the ultimate states. In addition, Fig. 3 also shows the investigated sections (A-A, B-B and C-C) during the tests, which would be discussed in detail later.

Fig. 4 shows the displacement transducers for measuring the deflections and interlayer slips. In particular, there were two symmetrically mounted transducers in transverse direction at the supports and loading positions, which was for checking load eccentricity.

Table 2 Concrete properties (MPa)

Curing age	NSN-1(52days)			NSN-2(48days)			NSD-1(55days)			NSD-2(59days)		
	f_c^*	f_t	E	f_c	f_t	E	f_c	f_t	E	f_c	f_t	E
7	48.0	3.0	-	<i>the same with NSN-1</i>								
28	59.1	3.8	41500									
test day	58.2	4.4	-	59.2	3.74	-	59.9	4.4	-	61.2	3.9	-

* f_c is the compressive strength; f_t is the tensile strength; E is the Young's modulus

Table 3 Steel and reinforcement properties (MPa)

Plate thickness or rebar diameter(mm)	4	5	6	8	R6	R8
f_{ay}^*	387	378	343	415	-	-
f_{au}	540	520	487	494	386	429

* f_{ay} is the yielding strength; f_{au} is the ultimate tensile strength

Fig. 5 shows the strain gauge distribution in the cross section A-A (Fig. 3), including the steel girder, the concrete slabs and the reinforcements. Such installation repeated at C-C section (Fig.3).

In addition, there were some strain gauges attached on both sides of steel webs at some positions of these sections. It was for checking the out-plane deformations. As to the section B-B (Fig. 3), only the steel bottom flange was mounted with strain gauges. Moreover, the crack width and the development were also recorded.

2.3 Material test

The material properties of concrete were tested at several concrete curing ages, such as 7-day, 28-day and the experiment day. The uniaxial compressive strength test used 150 mm cubic test specimens. The uniaxial tensile strength and Young's modulus tests used 40×40×160 mm specimens and 100×100×300 mm specimens, respectively. Table 2 summarizes the related test results, and some results with large error due to the specimen initial imperfection were not listed. Table 3 lists the tensile yielding and ultimate strength of the steel plates.

3. Test results

3.1 Failure mode

As shown in Fig. 6 that describes the specimen ultimate status, the failure modes generally consisted of the concrete cracks and steel parts yielding. The difference among the specimens was not obvious.

In particular, the tensile concrete cracks on the deck slab initiated at the early load stage and kept developing until thorough cracks appeared in the slab thickness direction. In

terms of the strain measurements at this moment, the embedded reinforcement had already yielded and the load on the concrete part redistributed to the steel parts. Such redistribution contributed to the steel flange yielding. At the ultimate status when the concrete slab nearly fractured because of tensile forces, the steel section and reinforcement yielded largely without significant buckling.

3.2 Load-deflection relationship

Fig. 7 summarizes the load-deflection relationships at the loading position of the specimens. The depicted deflections were the averages of measurements from the two symmetrically mounted displacement transducers as shown in Fig. 3. All the relationship curves included the elastic stage, the plastic hardening stage and the unloading stage. In the elastic stage, the girder stiffness respectively defined by the slopes of the secant lines between the origin and the points on the curves at specific load levels of 100 kN and 300 kN were listed in Table 4. These two stiffness values corresponded to the maximum crack width less and more than 0.2 mm. Based on the comparison as listed in Table 4, the double composite action and the higher reinforcement ratio contributed to a higher bending stiffness. Moreover, the effect of reinforcement ratio on the bending stiffness k_{300} appeared to be more obvious than k_{100} , probably because of that the embedded reinforcements contributed more when concrete cracks became larger.

With regard to the load-carrying capacity defined by the maximum applied load shown in Fig.7 and summarized in Table 4, the favorable effect of double composite action was obvious. The maximum load P_u applied on the specimen NSD-1 was 6% higher than specimen NSN-1. And the P_u on specimen NSD-2 was 12% higher than specimen NSN-2. The effect of double composite action on P_u was more obvious for the specimens with lower reinforcement ratio in the tests. Moreover, the deformations corresponding to P_u of the double composite specimens appeared to be slightly lower than the one of conventional composite specimens,

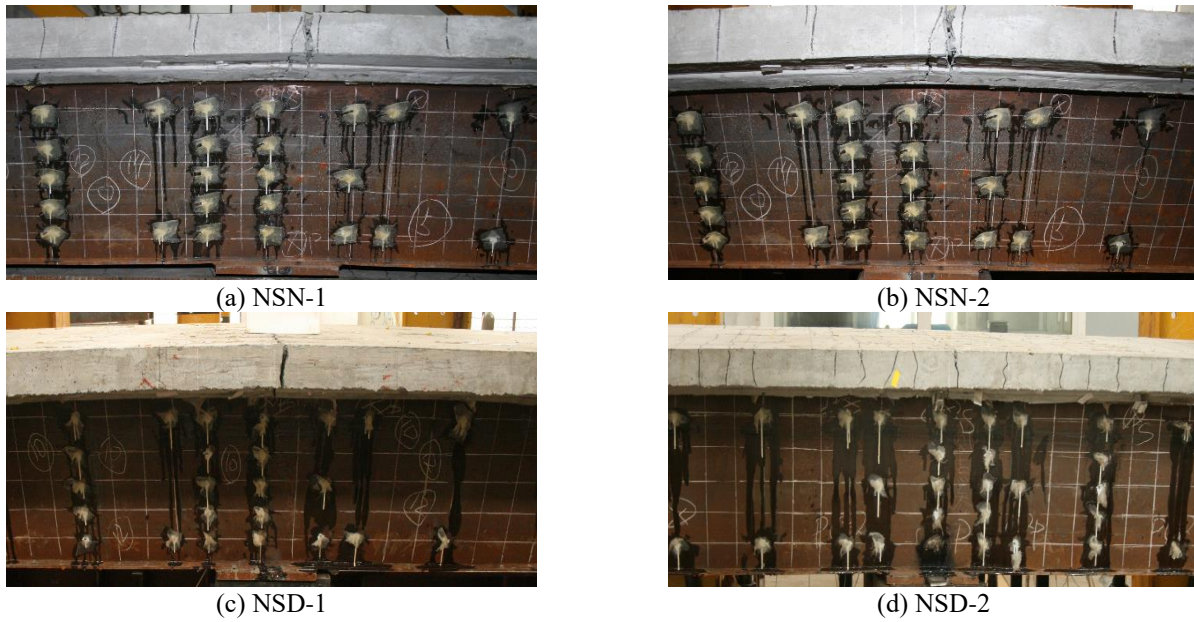


Fig. 6 Ultimate status of the test specimens. (Photos taken by Chen and Siwei)

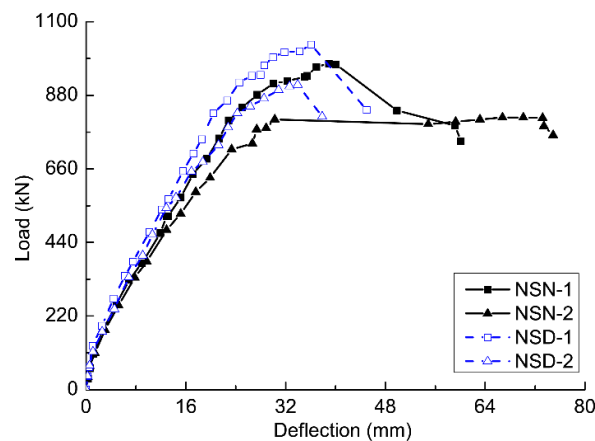


Fig. 7 The load-deflection relationships at the specimen loading positions

Table 4 Details of the bending stiffness and load-carrying capacity

specimen	(1)NSN-1	(2)NSN-2	(3)NSD-1	(4)NSD-2	(3)/(1)	(4)/(2)	(1)/(2)	(3)/(4)
k_{100} (kN/mm)*	99.2	89.4	115.4	117.1	1.16	1.31	1.11	0.99
k_{300} (kN/mm)*	51.1	45.0	58.3	50.4	1.14	1.12	1.14	1.16
P_u (kN)	975.1	813.2	1031.7	911.3	1.06	1.12	1.20	1.13

* k_{100} and k_{300} respectively denote the slopes of the secant lines from the origin to the points at 100 kN and 300 kN on the curves as shown in Fig. 7. P_u means the maximum load applied on the specimens at the ultimate state

indicating the double composite specimens tended to be comparatively less ductile but still in an acceptable range. As to the effect of reinforcement ratio, the P_u on specimen NSN-1 was 20% higher than the one on NSN-2, and the P_u on specimen NSD-1 was 13% higher than the one on NSD-2.

3.3 Crack features and reinforcement strains

Table 5 summarizes the measured maximum concrete crack width at several load steps. Accordingly, the crack width was sensitive to the reinforcement ratio in both of the NSN and NSD specimens, a higher reinforcement ratio

contributed to a smaller concrete crack width. On the other side, the influence of double composite action on the crack width was not remarkable.

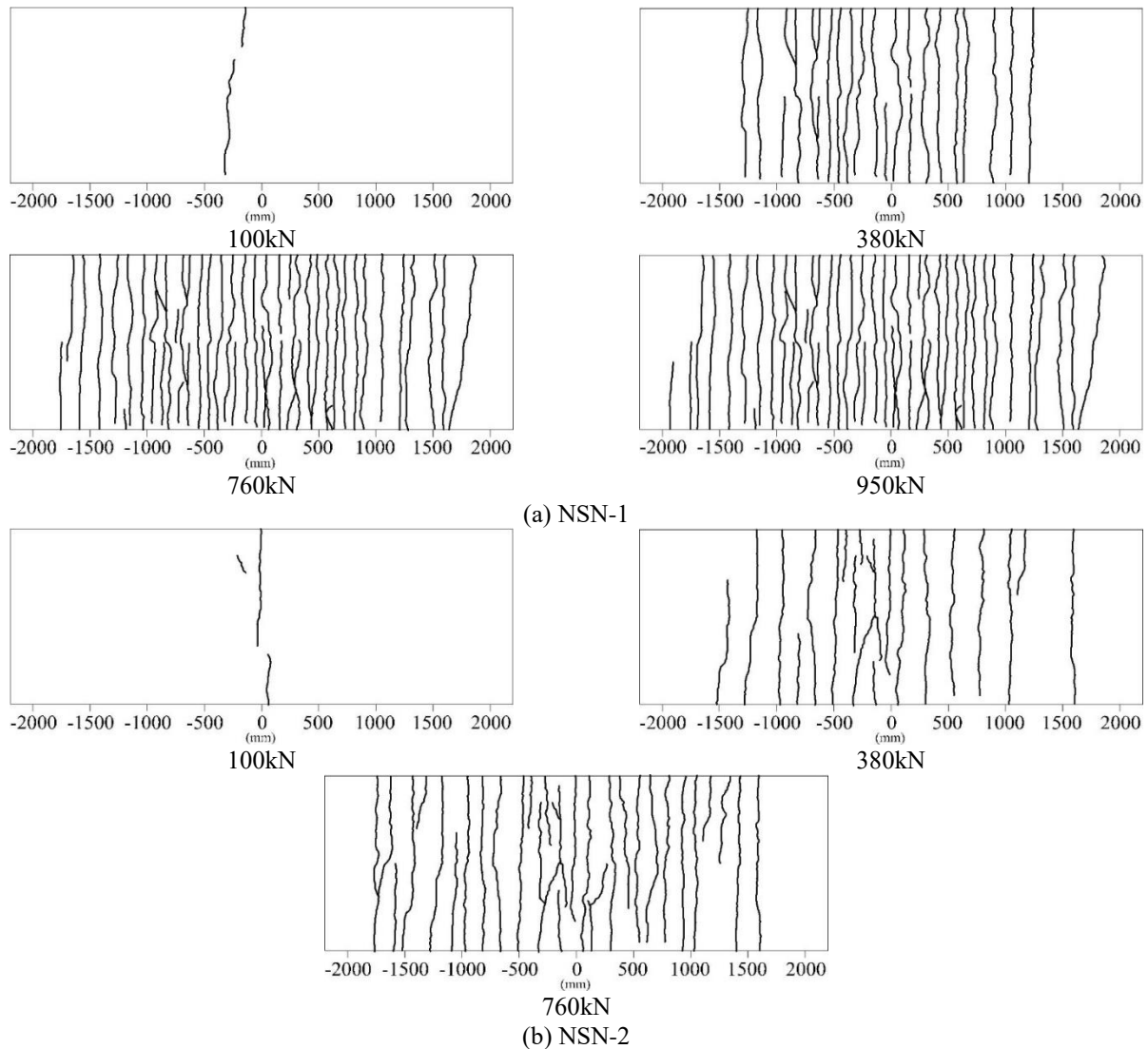
Furthermore, Fig. 8 illustrates the crack distributions on the concrete deck slabs at several load steps. The horizontal axis shows the longitudinal distances from the cracks to the center of the slab. According to the artificial visual observations, the initial cracking detected load level were respectively around 100 kN, 100 kN, 190 kN and 70 kN in NSN-1, NSN-2, NSD-1 and NSD-2.

These load levels were close to the exact initial cracking loads, but obviously not the exact ones due to the artificial errors. According to Fig. 8, all the cracks initialized from the slab centers and spread symmetrically along the longitudinal direction.

Based on the comparisons between the NSN specimens and between the NSD specimens, the higher reinforcement ratios tended to make the crack distributions on the NSN-1 and NSD-1 denser.

Table 5 The maximum concrete crack width development during the loading process (mm)

specimens	load steps				
	380 kN	530 kN	640 kN	760 kN	950 kN
NSN-1	0.22	0.25	0.29	0.37	0.6
NSN-2	0.47	0.51	0.68	1.08	—
NSD-1	0.22	0.27	0.27	0.33	0.66
NSD-2	0.36	0.49	0.54	0.9	—



Continued-

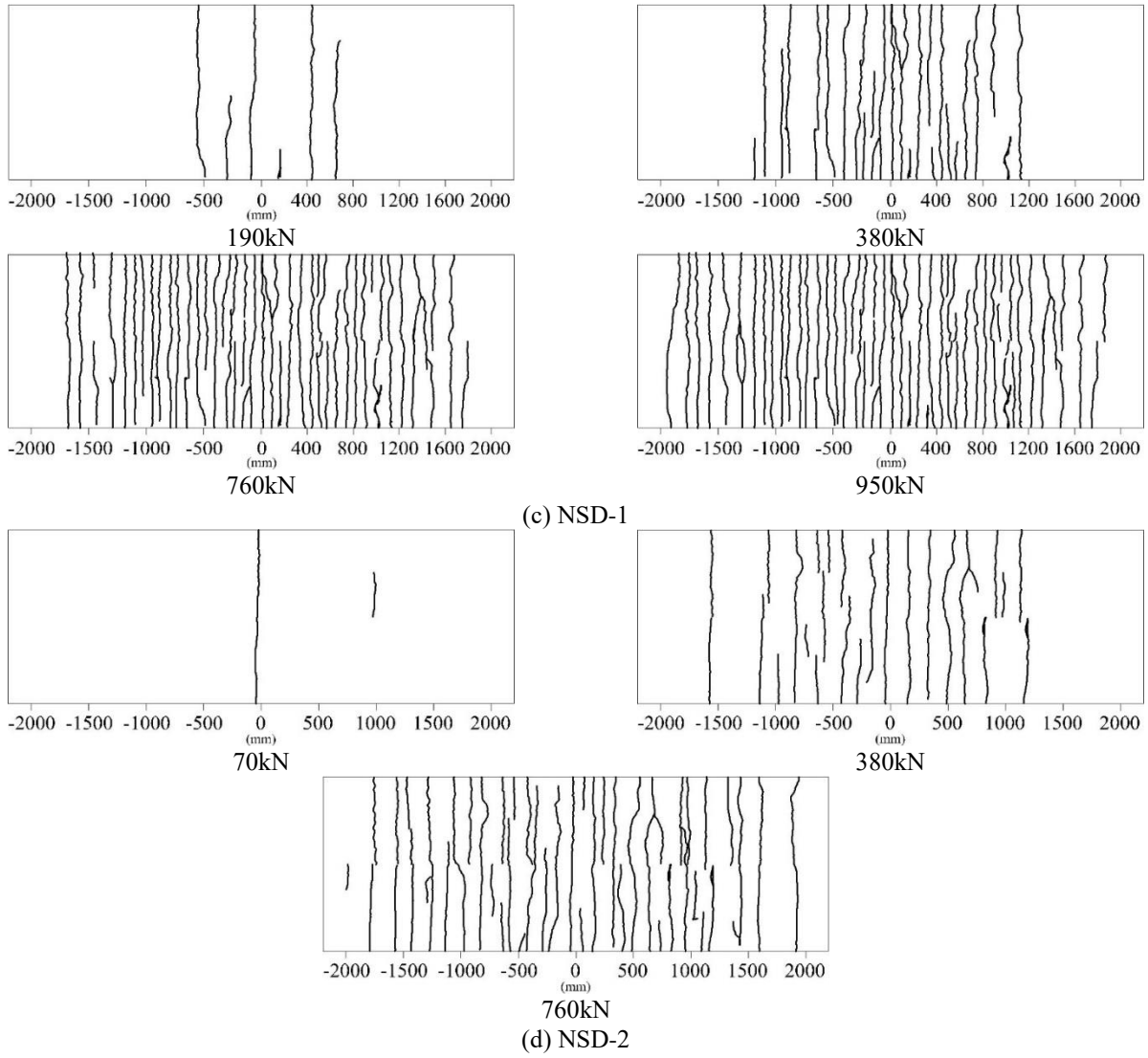


Fig. 8 The tensile concrete crack distributions at several load steps

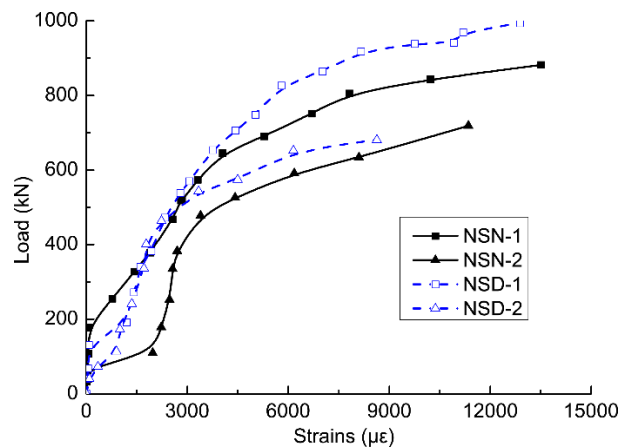


Fig. 9 The load-reinforcement strain relationships at the longitudinal centers of concrete deck slabs

And if comparing the NSN and NSD specimens with the same reinforcement ratio, the crack distribution appeared to be similar, which means the effect of double composite action on the crack distribution is not obvious.

Fig. 9 summarizes the load-strain relationships of reinforcements embedded in the concrete deck slabs at the specimen centers. These relationship curves included the intact, crack formation, stabilized cracking and post

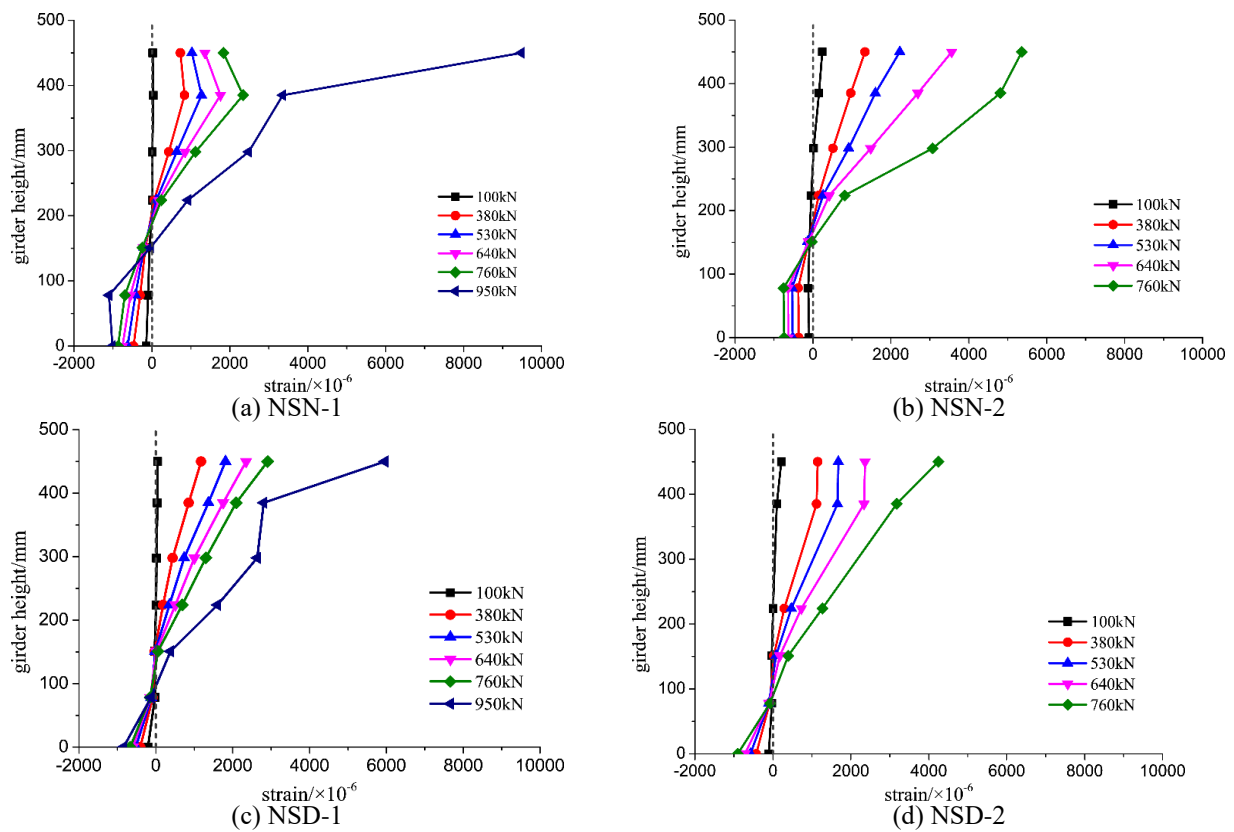
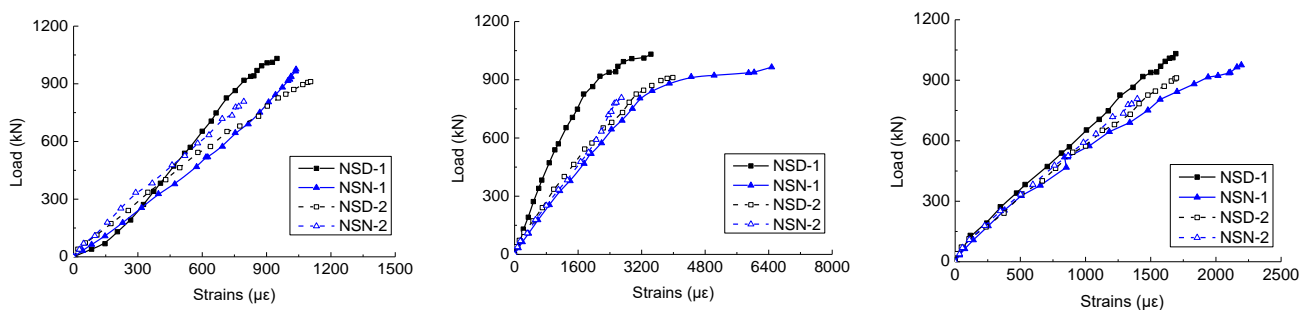


Fig. 10 The steel sectional strain distributions at A-A as shown in Fig. 3



(a) support Section A-A in Fig. 3

(b) near support Section B-B in Fig. 3

(c) a girder height Section C-C in Fig. 3

Fig. 11 The strain development at the steel bottom flange

yielding phases. The reinforcement strains were small and developed slowly until the crack initialized. Then the strains increased rapidly in the crack formation stage. In the following stabilized cracking and post yielding stage, the tension stiffening effect together with the reinforcement yielding can be observed. The cracks developed deeply into the concrete slab, leading to the tensile failure. In addition, the reinforcement strains developed more rapidly in the specimens with lower reinforcement ratio (NSN-2 and NSD-2).

3.4 The sectional strain distributions

Fig. 10 summarizes the steel part sectional strain distributions at the loading positions (Section A-A shown in Fig. 3). The distributions generally matched with the Plane Section Assumption, and the strain increment along with the load steps appeared to be larger in the specimens with lower reinforcement ratio.

Meanwhile, Table 6 lists the neutral axis height in terms of Fig. 10 at several load steps. Accordingly, the neutral axis position lowered down due to the additional bottom concrete slab or the lower reinforcement ratio in the deck

Table 6 The sectional neutral axis height during the loading process according to Fig.11 (mm)

Specimens	Load level (kN)					
	100	380	530	640	760	950
NSN-1	208	205	198	192	188	154
NSN-2	274	182	176	166	153	-
NSD-1	212	161	154	146	131	96
NSD-2	224	136	120	105	90	-

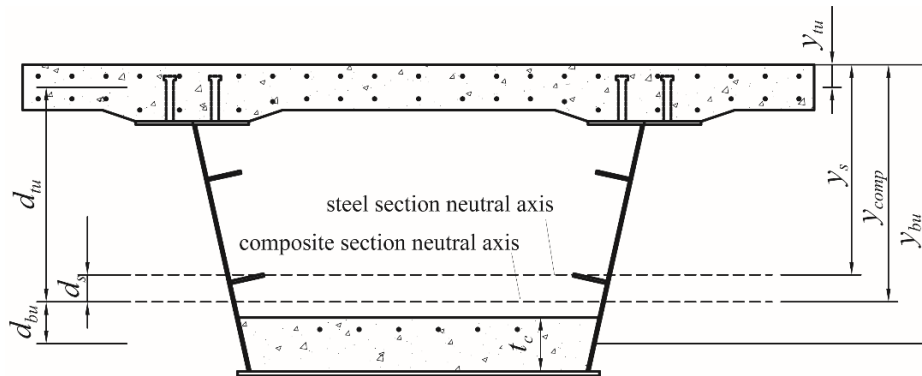


Fig. 12 The parameter illustration of the double composite section for the cracking moment evaluation (connectors on the bottom were not shown)

slab in general. Moreover, every specimen's sectional neutral axis dropped along the height during the loading process due to the concrete cracking.

Furthermore, Fig. 11 summarizes the compressive strain development at the steel bottom flange at several positions as shown in Fig. 3, including the sections of A-A (specimen center), B-B (near center) and C-C (1 times girder height away from the center). These plotted strains in each section were averages of the three gauges mounted on the steel bottom flange in the same section. Accordingly, the strains in NSD-1 were obviously lower than those in NSN-1 were, especially at A-A section. It shows that the additional bottom concrete slab assisted the steel bottom flange to support the compressive strains. However, such phenomenon was less obvious when comparing the strain development in NSD-2 and NSN-2, which had smaller reinforcement ratio and lower neutral axis height.

4. Evaluations of the double composite section

Although the double composite action is particularly good to prevent the steel buckling and increase the sectional stiffness, the additional concrete slab at the bottom may lower the sectional neutral axis height according to Table 6. Its detail effect on the tensile cracks of the concrete deck slab remains unclear. In this case, a further analytical study on the effect of the bottom concrete slab thickness on the cracking moment and load-carrying capacity was carried out. This is important to the rational design practice.

4.1 Cracking moment

The cracking moment, defined by the negative bending moment that initialize the first concrete crack on a slab, can be derived by Eq. (1).

$$\frac{f_t}{E_c} = \frac{M_{cr} y_{comp}}{E_s I} \quad (1)$$

Where M_{cr} is the cracking moment; f_t is the tensile strength of the concrete; E_s and E_c were the modulus of steel and concrete; y_{comp} is the distance from the upper fiber of the concrete deck slab to the composite sectional neutral axis; and I is the sectional bending moment of inertia. Particularly, y_{comp} can be derived by Eq. (2), where A_{tu} is the concrete deck slab area, A_{bu} is the bottom concrete slab area, A_s is the steel sectional area, n is the modulus ratio of concrete to steel, y_{tu} and y_{bu} are respectively the vertical distances from the slab centroids to the upper fiber of the composite section. It can be seen y_{comp} varies with A_{bu} which is determined by the dimensional size including the slab thickness t_c . Likewise, the sectional bending moment of inertia I , expressed by Eq. (3), also varies the slab thickness t_c . Fig. 12 illustrates the geometrical parameters for the evaluations in Eqs. (1)-(3).

$$y_{comp} = \frac{n(A_{tu} \cdot y_{tu} + A_{bu} y_{bu}) + A_s y_s}{n(A_{tu} + A_{bu}) + A_s} \quad (2)$$

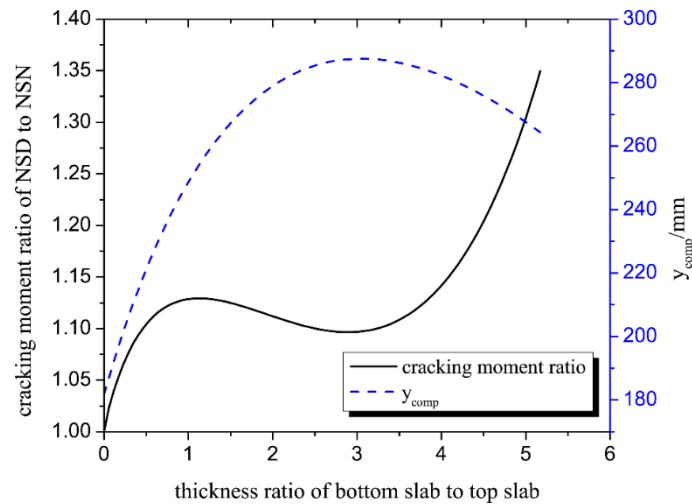


Fig. 13 The influences of bottom slab thickness on the cracking moment and y_{comp} value

Table 7 The cracking moment comparison between the test results and theoretical evaluations (kN.m)

specimen	(1)NSN-1	(2)NSN-2	(3)NSD-1	(4)NSD-2	(3)/(1)	(4)/(2)	(1)/(2)	(3)/(4)
(a) Theoretical estimations	210.0	172.6	237.6	202.9	1.13	1.18	1.22	1.17
(b) Test results	122.5	122.5	232.8	85.75	1.90	0.90	1.00	2.11
(b)/(a)	0.58	0.71	0.98	0.42				

$$I_{comp} = n(I_{tu} + I_{bu} + A_{tu}d_{tu}^2 + A_{bu}d_{bu}^2) + I_s + A_s d_s^2 \quad (3)$$

Assuming all the geometrical parameters in Eqs. (1)-(3) except the bottom slab thickness t_c were constants of which the specific values can be found in Fig. 1, the relationship between t_c and M_{cr} can be summarized in Fig. 14 through calculations. The horizontal axis shows the bottom slab thickness normalized by the deck slab thickness in a composite section, the left vertical axis shows the cracking moment normalized by the corresponding value of a conventional composite section without an additional bottom concrete slab. Meanwhile, a plotted dash line valued through the right vertical axis reflects the y_{comp} variation feature.

The cracking moment curve in Fig. 13 contains three stages. When thickness ratio is less than 1 which means the bottom slab thickness t_c is smaller than the deck slab thickness, the cracking moment can be improved by the bottom slab. When the thickness ratio goes beyond 1, the cracking moment decreases with the bottom slab thickness mainly due to a continuing downward translation of the sectional neutral axis, which is reflected by y_{comp} . When the bottom slab thickness goes beyond nearly 3 times to the deck slab thickness, the cracking moment increases again.

Table 7 summarizes the cracking moment comparison between the test and the evaluation results according to Eqs. (1)-(3). It shows that the bottom slab did not drive a significant unfavorable effect on the cracking moment. As to the difference between the test and evaluation results in particular, one reason might be the test observation errors. It is noteworthy that the cracking loads in the test were not

very accurate due to the artificial observation errors. The accurate ones may be lower. Moreover, the tensile strength of the concrete used in the theoretical calculation was around 4.0 MPa based on Table 1. However, it might not be the same with the concrete in the test specimens due to a comparatively different curing environment.

4.2 Negative bending-carrying capacity

As to the negative bending-carrying capacity evaluation, there are two possible cases as shown in Fig. 14 in terms of the sectional neutral axis position. And the double composite section mentioned hereafter belongs to the Class 1 or Class 2 cross section as specified in Eurocode 4(2005), which means a full plastic sectional stress distribution can be achieved.

Case 1: the full plastic neutral axis in the web above the bottom concrete slab (Fig. 14(a))

As shown in Fig. 14(a), the full plastic sectional stress distribution can decompose into two parts, including a stress distribution on the pure steel girder and an equivalent stress superimposition. f_r , f_s , and f_c are respectively the yielding strength of reinforcement, yielding strength of steel and the compressive strength of concrete. Accordingly, the sectional bending-carrying capacity M_{pl} is the sum of M_s and M_r as expressed by Eq. (4) where M_s is the sectional bending-carrying capacity of steel girder and M_r is the bending-carrying capacity contributed by the equivalent superimposition part. Based on Fig. 14(a), M_r correlates with the bottom concrete slab thickness t_c .

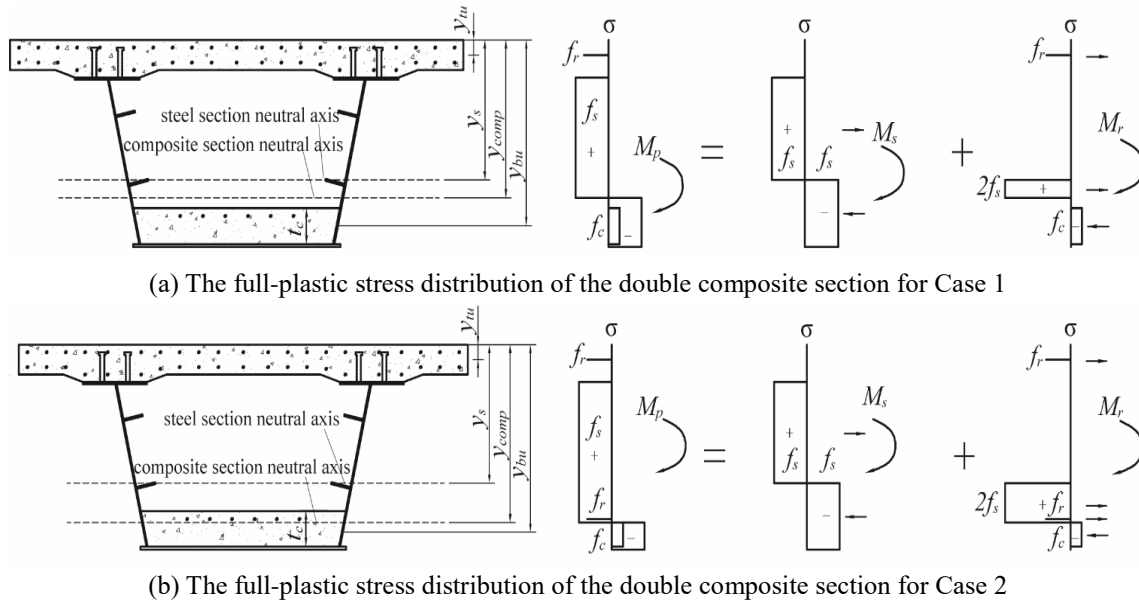


Fig. 14 The full-plastic stress distribution of the double composite section. (connectors on the bottom were not shown)

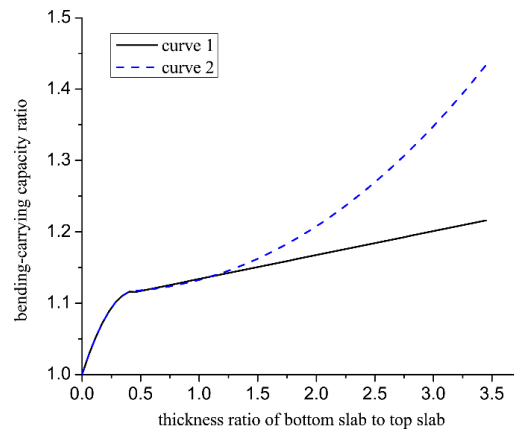


Fig. 15 The influence of bottom slab thickness on the sectional negative bending-carrying capacity

$$M_{pl} = M_s + M_r \tag{4}$$

Case 2: the full plastic neutral axis in the bottom concrete slab (Fig.14(b))

As to the Fig. 14(b), the full plastic section stress distribution consists of two parts as well, including the stress distribution on the pure steel girder and an equivalent stress superimposition. The difference between Fig. 14a and 14b is the derivation of M_r . When the plastic neutral axis falls down into the bottom slab, the concrete above the axis has little contribution to the bending-carrying capacity whereas the embedded reinforcements which bear the tensile yielding stress should be considered.

According to the evaluation results of the above-mentioned two cases, the relationship between the bottom concrete slab thickness t_c and the negative bending-carrying capacity M_{pl} can be depicted by Fig. 15. Each depicted curve contains the above-mentioned axis two cases. The

difference between the two curves are the evaluation preconditions. Curve 1(solid line) was derived based on a precondition that the longitudinal reinforcement section area in the bottom slab is constant And Curve 2(dash line) was derived based on a precondition that the reinforcement ratio of the bottom slab is constant, which means the reinforcement section area increases with the bottom slab thickness t_c . The horizontal axis in Fig. 15 shows the ratio of the bottom concrete slab thickness t_c to the upper deck slab thickness. And the vertical axis shows the ratio of the corresponding bending-carrying capacity M_{pl} to the one of a conventional composite section without an additional bottom concrete slab.

As to the curves in Fig. 15 in particular, when the thickness ratio is less than 0.4, the full plastic neutral axis is above the bottom concrete slab (Case1). The two curves coincide with each other since the evaluation precondition difference mentioned above has little effect when the whole

Table 8 The bending-carrying capacity comparison between the test results and theoretical estimations (kN.m)

specimen	(1)NSN-1	(2)NSN-2	(3)NSD-1	(4)NSD-2	(3)/(1)	(4)/(2)	(1)/(2)	(3)/(4)
(a) Theoretical estimations	1122.9	985.0	1283.5	1065.0	1.14	1.08	1.14	1.21
(b) Test results	1097.0	914.9	1160.7	1025.2	1.06	1.12	1.20	1.13
(b)/(a)	1.06	1.01	0.98	1.05				

bottom concrete slab is under compression. When the thickness ratio goes beyond 0.4, the full plastic neutral axis falls down into the bottom slab (Case 2). The contribution of the embedded reinforcement under tension results to different curves by different evaluation preconditions as mentioned. According to the depicted relationship curves, a slab thickness ratio around 0.4 can improve the sectional bending-carrying capacity by around 10%, and a 1.0 slab thickness ratio can improve the sectional bending-carrying capacity by 12%.

Table 8 summarizes the bending-carrying capacity comparison between the test results and the evaluations. Generally, the test results matches well with the cracking moment estimations, confirming the theoretical estimations on the sectional bending-carrying capacity.

5. Conclusions

The mechanical behavior of double composite action in the negative flexural region of a continuous composite girder was studied. Meanwhile, the structural rationality of the bottom slab in the double composite section was analyzed as well. The results can be summarized as follows.

- According to the test results, the failure modes consisted of the large concrete cracks and the steel parts yielding. And the bending stiffness and capacity improvements by the double composite action can be confirmed.

- Furthermore, the effect of double composite action on the tensile crack distribution on the concrete deck was not obvious, while the higher reinforcement ratio resulted to a denser crack distribution.

- According to the observation on the sectional strain distribution in the tests, the sectional neutral axis could be lower due to the additional concrete at the bottom or the lower reinforcement ratio. Nevertheless, the additional bottom concrete slab was able to assist the steel bottom flanges to support the compressive stress.

- According to the analyzed influences of the bottom concrete slab thickness on the cracking moment and the bending-carrying capacity, the thickness of the bottom concrete slab can be around the thickness of the concrete deck slab for the design practice. This configuration of additional concrete slab in the bottom may contribute to a nearly 15% improvement of the cracking moment and 12% improvement of the sectional bending-carrying capacity.

Acknowledgements

This research is sponsored by the National Key R&D Program of China (No. 2017YFC0703402), National Natural Science Foundation of China (51978501), Shanghai Pujiang Project (No. 18PJ1410300), Tongji Civil Engineering Peak Discipline Plan and China Fundamental Research Funds for the Central Universities. These supports are gratefully acknowledged. Meanwhile, many thanks to Mr. Hang SU, Mr. Yangcong LOU and Mr. Zhehao Hou for their contributions to this paper.

References

- AASHTO (2012), LFRD bridge design specifications, 4th edition, American Association of State Highway and Transportation Officials.
- Chen S. and Jia Y. (2010), "Numerical investigation of inelastic buckling of steel-concrete composite beams prestressed with external tendons", *Thin-Walled Struct.*, **48**(3), 233-242. <https://doi.org/10.1016/j.tws.2009.10.009>.
- Chen, S.M., Wang, X and Jia, Y. (2009), "A comparative study of continuous steel-concrete composite beams prestressed with external tendons: experimental investigation", *J. Constr. Steel Res.*, **65**(7), 1480-1489. <https://doi.org/10.1016/j.jcsr.2009.03.005>.
- China National Standard, GB50917-2013. Code for design of steel and concrete composite bridges. [in Chinese]
- Committee of steel structure, JSCE. (2007), Standard specification for steel and composite structures (Design edition). [in Japanese].
- Eurocode 4: Design of composite steel and concrete structures, Part 2: General rules and rules for bridges (2005), European Committee for Standardization, Brussels.
- Hamoda, A., Hossain, K., Sennah, K., Shoukry, M. and Mahmoud, Z. (2017), "Behaviour of composite high performance concrete slab on steel I-beams subjected to static hogging moment", *Eng. Struct.*, **140**, 51-65. <https://doi.org/10.1016/j.engstruct.2017.02.030>.
- Jiang, Y.C., Hu, X.M., Hong, W. and Wang, B.L. (2016), "Experimental study and theoretical analysis of partially encased continuous composite beams", *J. Constr. Steel Res.*, **117**, 152-160. <https://doi.org/10.1016/j.jcsr.2015.10.009>.
- Kim, C.E., Kim, J.K., Yun, N.R. and Shim, C.S. (2015), "Structural Behavior of a continuous composite truss with a composite bottom chord", *J. Constr. Steel Res.*, **105**, 1-11. <https://doi.org/10.1016/j.jcsr.2014.11.001>.
- Liang, H.Y., Qiang, X.Y., Si, L.L. and Ying, Y. (2018), "Mechanical Behavior of Steel-HFRC Composite Girders", *J Bridge Eng.*, **23**(10), [https://doi.org/10.1061/\(ASCE\)BE.1943-5592.0001275](https://doi.org/10.1061/(ASCE)BE.1943-5592.0001275).
- Liang, Q.Q., Uy, B., Bradford, M.A. and Ronagh, H.R. (2004), "Ultimate strength of continuous composite beams in combined bending and shear", *J. Constr. Steel Res.*, **60**(8), 1109-1128.

- <https://doi.org/10.1016/j.jcsr.2003.12.001>.
- Lin, W.W., Yoda, T. and Taniguchi, N. (2014). "Application of SFRC in steel-concrete composite beams subjected to hogging moment", *J. Constr. Steel Res.*, **101**, 175-183. <https://doi.org/10.1016/j.jcsr.2014.05.008>.
- Lu, Y. and Ji, L. (2018), "Behavior of optimized prestressed concrete composite box-girders with corrugated steel webs", *Steel Compos. Struct.*, **26**(2), 183-196. <https://doi.org/10.12989/scs.2018.26.2.183>.
- Moscoso, A.M., Tamayo, J. and Morsch, I.B. (2017), "Numerical simulation of external pre-stressed steel-concrete composite beams", *Comput. Concrete*, **19**(2), 191-201.
- Saul, R. (1996), "Bridges with double composite action", *Struct. Eng. Int.*, **6**(1), 31-36. <https://doi.org/10.2749/101686696780496067>.
- Shao, X.D. and Deng, L. (2016), "Steel-UHPC lightweight composite bridge girders for long-span bridges". Maintenance, Monitoring, Safety, Risk and Resilience of Bridges and Bridge Networks, 363.
- Shim, C.S., Wang, J.W., Chung, C.H. and Lee, P.G. (2011), "Design of double composite bridges using high strength steel", *Proceedings of the 12th East Asia-Pacific conference on structural engineering and construction*, Procedia Engineering, **14**, 1825-1829.
- Wang, J., Xu, Q., Yao, Y., Qi, J. and Xiu, H. (2018), "Static behavior of grouped large headed stud-UHPC shear connectors in composite structures", *Compos. Struct.*, **206**, 202-214. <https://doi.org/10.1016/j.compstruct.2018.08.038>.
- Wang, Z., Nie, X., Fan, J., Lu, X. and Ding, R. (2019), "Experimental and numerical investigation of the interfacial properties of non-steam-cured UHPC-steel composite beams", *Constr. Build. Mater.*, **195**, 323-339. <https://doi.org/10.1016/j.conbuildmat.2018.11.057>.
- Xu, C., Su, Q. and Masuya, H. (2017), "Static and fatigue performance of stud shear connector in steel fiber reinforced concrete", *Steel Compos. Struct.*, **24**(4), 467-479. <https://doi.org/10.12989/scs.2017.24.4.467>.